Kinematic and Acoustic Similarities of Separated Turbulent Boundary Layers

Alexandre Suryadi *
German Aerospace Center (DLR), 38108 Braunschweig, Germany

This study proposes a similarity model for separated turbulent boundary layers as a function of the outer flow parameters, the velocity associated with the maximum local mean shear $U_m = \sqrt{\tau_m/\rho}$, and the reduced wall-normal coordinate. By using this similarity model, the outer layer profiles are scaled for approximately 70–80% of the boundary layer height. A corresponding similarity model of the far-field sound pressure levels and surface pressure autospectrum was derived. The proposed scaling shows less variability than the canonical trailing-edge noise scaling within a range of the freestream velocity and airfoil's angle of attack. The scaling of the surface pressure autospectrum reveals that the viscous and inertial timescales are of the same order of magnitude, which suggests strong turbulent dissipation in the separated turbulent boundary layer that results in the steep roll-off of the autospectrum in the mid-frequency range.

Nomenclature

a_∞	=	speed of sound
b	=	span length
B	=	Schofield-Perry integral layer thickness
c	=	chord length
d	=	diameter
f	=	frequency
f_m	=	one-third octave band center frequency
$f(\eta)$	=	self-similar velocity profile of Schüle-Rossignol. Eq. (3)
L	=	position of τ_m from the profile's point of origin
$L_{p,1/3}$	=	one-third octave band sound pressure level
l_{ref}	=	reference length, $l_{ref} = R^2/b$
M	=	Mach number

*Research Engineer, Institute of Aerodynamics and Flow Technology, Technical Acoustics. Lilienthalplatz 7, 38108 Braunschweig, Germany. alexandre.suryadi@dlr.de, AIAA member

P	=	mean pressure
q_e	=	local dynamic pressure, $q_e = 0.5\rho U_e^2$
r_z^*	=	distance of two points in the spanwise direction
R	=	distance of the noise source to an observer
R_T	=	ratio of inertial to viscous timescales
Re_δ	=	Reynolds number, $Re_\delta = U_e\delta/\nu$
S_{FF}	=	narrow band far-field noise spectrum
St	=	Strouhal number
U	=	mean streamwise velocity
$\bar{U}_c$	=	mean convection velocity
U_e	=	mean streamwise velocity at boundary layer thickness
U_m	=	velocity associated with maximum shear stress, Eq. (1)
U_{ref}	=	arbitrary velocity scale, 1 m/s
U_s	=	Schofield-Perry velocity scale
u_τ	=	friction velocity, $u_\tau = \sqrt{\tau_w/\rho}$
u, v, w	=	fluctuating velocity components
x, y, z	=	streamwise, wall-normal, and spanwise direction
α	=	angle of attack
γ_p	=	fraction of time that the flow near the wall is in the downstream direction
δ	=	boundary layer thickness
δ_0	=	height of zero-velocity streamline
δ_1	=	displacement thickness
δ'	=	characteristic length scale
ΔU_i	=	mean streamwise velocity difference of the inner region, Eq. (19)
ΔU_o	=	mean streamwise velocity difference of the outer region, Eq. (22)
η	=	reduced wall-normal coordinates, Eq. (4)
ℓ_z	=	spanwise integral length scale
ν	=	kinematic viscosity
$\hat{\Pi}$	=	wake parameter
ρ	=	density
τ_m	=	local maximum shear stress
τ_w	=	local wall shear stress

Φ_{pp} = surface pressure spectrum

Subscripts

g = geometric

i = inner region

l = linear region

m = maximum mean shear

max = maximum

model = model

o = outer region

∞ = freestream

Superscripts

$*$ = dimensional parameters

$+$ = normalization with shear variables

I. Introduction

For fluid machinery to operate consistently, it is designed to avoid flow separation. When it occurs flow separation lead to stalling and aerodynamic performance suffers. The operational conditions of most fluid machinery are in the steady-state. However, wind turbine operations rely on the local and temporal atmospheric conditions. This transience could lead to the possibility of separated flow over the turbine blades. The transient conditions may be relatively short compared to the operational lifetime of a wind turbine, but flow separation can lead to increased noise that may further impact the surrounding neighborhoods. For providing noise safety margins in wind turbine certification, it is essential that the extraneous noise sources, which among them is due to flow separation, are included. The topic of this paper is to develop similarity scalings for future prediction of flow separation noise.

To observe flow separation, one can trigger it using a discontinuous wall, such as a backward-facing step, using an oscillating wall, or using a smooth, continuous surface where the flow is affected by an adverse pressure gradient, such as a two-dimensional wing model at a high angle of attack, a bluff-body, or a diffuser wall. Schewe [1] classified flow separation of the latter case into three general categories (1) subcritical, laminar separation that develops into a turbulent wake [2, 3], (2) supercritical, laminar separation with downstream reattachment and transition to turbulence [4–9], and (3) transcritical, turbulent flow separation [10–15].

Winkelman and Barlow [16] visualized the topology of a separated turbulent boundary layer of a two-dimensional wing model using oil-flow visualization. The oil flow pattern consists of a saddle structure and focus points on either side. These structures are connected by bifurcation lines coming out from the saddle point. This flow pattern is commonly

called a *stall cell* and the bifurcation lines as *flow separation lines*. Depending on the ratio of the chord length and the span length of the model, the mushroom structure repeats itself. Winkelman and Barlow observed that the first appearance of a stall cell is at a pre-stall angle. Despite the three-dimensionality of the flow pattern, Shiloh et al. [12] measured the transverse velocity of a separated turbulent boundary layer and noted that even though the mean flow is three-dimensional, the streamwise mean flow is the main source of momentum and kinetic energy. Here, the mean process refers to the time-averaged process.

Simpson et al.[10] describe flow separation as a process that develops gradually along the streamwise, instead of as an event. This process is expressed by the probability of the flow near the wall is in the downstream direction, γ_p.

- Incipient Detachment (ID): the reverse flow occurs 1% of the sampled time, $\gamma_p = 0.99$
- Intermittent Transitory Detachment (ITD): the reverse flow occurs 20% of the sampled time, $\gamma_p = 0.8$
- Transitory Detachment (TD): the reverse flow occurs 50% of the sampled time, $\gamma_p = 0.5$
- Detachment (D): where the mean wall shear stress is zero

The flow is said to be separated in the classical sense during and after transitory detachment. The last point in the list above defines the classical separation point. Downstream of the separation point, the mean wall shear stress continues to decrease to a negative value and the streamwise mean pressure gradient is approximately zero.

A. Mean velocity scaling

Clauser [17] conducted the earliest work of similarity analysis of turbulent boundary layer under an adverse pressure gradient. Measurements were performed in conditions where the mean streamwise pressure gradient is inversely proportional to the wall shear stress, τ_w. This condition is defined by the Clauser parameter $\delta'/\tau_w \mathrm{d}P/\mathrm{d}x =$ constant, where δ' is a characteristic length scale to represent the boundary layer thickness. Maciel et al. [18] studied an equilibrium turbulent boundary layers under adverse pressure gradient leading to flow separation. Approaching flow separation, both mean velocity and Reynolds stress profiles can be scaled with δ and $U_e\delta_1/\delta$, where δ is the boundary layer thickness, δ_1 is the displacement thickness, and U_e is the mean streamwise velocity at a wall-normal position $y = \delta$.

One scaling approach for the prediction of flow separation eventuality was proposed by Perry and Schofield [19] using scales based on the local maximum shear stress, τ_m,

$$\begin{aligned} U_m &= \sqrt{\frac{\tau_m}{\rho}} \\ U_s &= 8\frac{B}{L}U_m \\ B &= 2.86\delta_1\frac{U_e}{U_s} \end{aligned} \tag{1}$$

where U_m is a velocity scale based on τ_m, U_s is the Schofield-Perry velocity scale, B is the Schofield-Perry integral

layer thickness, and L is the distance of τ_m from the origin of profile. Schofield [20] applied this similarity law to the separating flow of Simpson et al. [11]. He used locations in the transitory detachment region, where these datapoints are located at 130in. $< x <$ 144in., where $x = 0$ was defined at the leading edge of their test section. The model works when the point of origin is shifted to the zero velocity streamline [20].

Schüle and Rossignol [21] used the reduced wall-normal coordinate with the point-of-origin at the zero velocity streamline. Their similarity profile of a detached two dimensional turbulent boundary layer is a modification of the Coles' law of the wake.

$$\frac{U(\eta)}{U_e} = \hat{\Pi} f(\eta) + g(\eta) + h(\eta, \hat{\Pi}) \tag{2}$$

where $\hat{\Pi}$ is the wake parameter. The three functions in Eq. (2) are given as

$$\begin{aligned} f(\eta) &= \sin^2\left(\frac{\pi}{2}\eta\right) \\ g(\eta) &= \frac{a_1}{\pi - 4}\left[2 + (\pi - 4)\eta - (\pi - 2)\eta^2 - 2\cos\left(\frac{\pi}{2}\eta\right)\right] \\ h(\eta, \hat{\Pi}) &= \frac{1 - \hat{\Pi}}{2}\left[\tanh(\alpha\eta - \beta) + 1\right] \end{aligned} \tag{3}$$

With the last function, $h(\eta, \hat{\Pi})$, is a non-physical function to fit the model of the boundary conditions with $\alpha = 12.5$ and $\beta = 9.5$ given heuristically. The wall-normal coordinate, η, has its point-of-origin at $U(y = \delta_0) = 0$, where δ_0 is the height of the reverse flow layer.

$$\eta = \frac{y - \delta_0}{\delta - \delta_0} \tag{4}$$

and the parameter a_1 is the non-dimensional kinematic shear at the point-of-origin

$$a_1 = \frac{1}{U_e}\left.\frac{\mathrm{d}U}{\mathrm{d}\eta}\right|_{\eta=0} \tag{5}$$

This similarity poses an open problem as the application of the boundary conditions

$$U(\eta = 0) = 0\,; \qquad U(\eta = 1) = U_e \tag{6}$$

leads to

$$\begin{aligned} h(\eta = 0, \hat{\Pi}) = 0\,; \quad h(\eta = 1, \hat{\Pi}) = 1 - \hat{\Pi}; \\ h'(\eta = 0, \hat{\Pi}) = 0\,; \quad h'(\eta = 1, \hat{\Pi}) = 0 \end{aligned} \tag{7}$$

giving the value $\hat{\Pi}$ indeterminable.

B. Trailing-edge noise scaling

In determining far-field noise, it is important to understand the surface pressure fluctuation of the incident turbulent field. Blake [22] derived the Poisson equation of the pressure fluctuation of a zero pressure gradient boundary layer by assuming the dominant term is the interaction of the mean shear with turbulence. A dimensional analysis reveals the contribution of each region of the velocity profile to the surface pressure autospectrum. The outer layer turbulence is associated with the inertial range, which has a dependency of f^2 in the surface pressure autospectrum, the logarithmic or overlap region with f^{-1} dependency, and the viscous sub-layer is associated with the dissipative range with f^{-5} dependency. By using flow simulations as inputs, Blake's equation can be used to calculate the surface pressure cross-spectrum and the trailing-edge noise [23]. This technique is of interest in airframe noise research [24, 25]. Schüle and Rossignol [26] used Blake's equation for the prediction of separated flow noise. They reasoned that the contribution to far-field noise is from the outer, downstream moving flow, not from the near-wall, reverse flow region, based on far-field noise measurements showing increasing spectral level towards lower frequency.

Another scaling that is important in the study of aeroacoustics is the surface pressure scaling, from which the far-field noise scaling can be derived. Several well-regarded works on this topic are the general study of airfoil self-noise by Brooks et al. [27], the surface pressure measurement of attached turbulent boundary layer for trailing edge noise prediction by Brooks and Hodgson [28] and the surface pressure measurement in a separating turbulent boundary layer by Simpson et al. [29]. The trailing-edge noise and flow separation noise scales with U_e^5 [27, 28], whereas in Simpson et al. flow separation noise is normalized with τ_m^2. The fifth-power law scales the classical trailing-edge noise well, but it does not correctly scale flow separation noise. This contradiction indicates that different parameters may govern the separated boundary layer.

This paper focuses on the development of a scaling method that addresses the mean and turbulent velocity profiles, surface pressure autospectra, and far-field noise spectra for turbulent boundary layers in the detached state, or downstream of the separation point.

II. Similarity of the mean velocity profile

In this and the following sections, the dimensional variables are denoted by an asterisk, *, and non-asterisk variables are non-dimensional variables. This section will detail the derivation of the scaling. First, the flow parameters are non-dimensionalized using the boundary layer thickness δ^* and the velocity at the boundary layer thickness U_e^*. Then U_m^*, the local maximum mean shear velocity, is defined, and the boundary layer parameters are normalized with it. Finally, the dataset used for building the model is presented.

This study proposes a similarity model using the local maximum mean shear velocity, similar to Schofield-Perry, and the reduced wall-normal coordinate, where the point of origin is above the wall at the position of the zero mean velocity in the separated boundary layer. Similarity is sought for the region above the reverse flow layer, following the

approach by Schüle and Rossignol [21]. The flow is assumed to be incompressible, statistically stationary, and effectively two-dimensional. In studying flow separation a wind-turbine rotor blade at the 75% outboard section, the boundary layer is assumed to transition to turbulent before separation. Schüle and Rossignol [26] measured the spanwise variation of the mean velocity profile of the separated turbulent boundary layer of a DU96-W-180 wing model with a 7-hole pressure probe at $\alpha = 14°$ at approximately 1% chord length, c, behind the trailing edge. Laminar to turbulent transition was forced by using zig-zag tripping at the chordwise position from the leading-edge $x^*/c^* = 0.05$ on the suction side and $x^*/c^* = 0.10$ on the pressure side. The spanwise length of the measurement domain was 360 mm, chord-normal mean velocity profiles were measured at 15 mm steps in the spanwise. The vertical length of the measurement domain was determined to fit the shear layer of the near wake of the trailing edge. From the 7-hole probe, the mean velocity components outside the reverse flow layer can be determined. The maximum spanwise variation of the mean streamwise velocity, $dU^*/dz^* = 6.8 \times 10^{-6} U_e^*/\delta^*$, is smaller than its chord-normal variation, $dU^*/dy^* = 0.0024 U_e^*/\delta^*$. The maximum of the spanwise mean velocity constitutes to 2% of the mean streamwise velocity.

A. Non-dimensionalized variables

The local mean streamwise velocity, U^*, and position in the wall-normal direction, y^*, are non-dimensionalized with the local U_e^* and δ^*, respectively. The boundary layer thickness is defined as the height of the boundary layer where U^* is equal to 99% of the potential flow velocity.

$$U = \frac{U^*}{U_e^*}; \quad y = \frac{y^*}{\delta^*} \tag{8}$$

The maximum shear velocity U_m^* of the local mean velocity profile is given as

$$U_m^* = \sqrt{\frac{\tau_m^*}{\rho^*}} = \sqrt{\nu^* \left.\frac{\mathrm{d}U^*}{\mathrm{d}y^*}\right|_{\max}} \tag{9}$$

In attached turbulent boundary layers, the maximum shear stress coincides with the wall shear stress. However, for separated turbulent boundary layers, the wall shear stress is defined as negative. Therefore the maximum is defined to be above the wall.

B. Shear normalized variables

Similar to the *law-of-the-wall* the velocity profile is normalized by U_m^* and the wall-normal direction by U_m^*/ν^*. We will loosely symbolize these normalized variables as U^+ and y^+.

$$\begin{aligned} U^+ &= \frac{U^*}{U_m^*} = \frac{U^*}{\sqrt{\nu^* \mathrm{d}U^*/\mathrm{d}y^*_{\max}}} \\ &= \sqrt{Re_\delta}\frac{U}{\sqrt{dU/dy_{\max}}} \end{aligned} \tag{10}$$

$$\begin{aligned} y^+ &= \frac{y^* U_m^*}{\nu^*} = y\frac{\delta^*}{\nu^*}\sqrt{\frac{\nu^* U_e^*}{\delta^*}}\sqrt{\left.\frac{dU}{dy}\right|_{\max}} \\ &= y\sqrt{Re_\delta}\sqrt{\left.\frac{dU}{dy}\right|_{\max}} \end{aligned} \tag{11}$$

Where $Re_\delta = U_e^*\delta^*/\nu^*$. The non-dimensional form of the maximum shear velocity can be defined as

$$U_m = \sqrt{\left.\frac{dU}{dy}\right|_{\max}} = \sqrt{Re_\delta}\frac{U_m^*}{U_e^*} \tag{12}$$

substituting Eq. (12) to Eqs. (10) and (11) leads to $U^+ = \sqrt{Re_\delta}U/U_m$ and $y^+ = y\sqrt{Re_\delta}U_m$, respectively.

C. Dataset

In the present study separated flow cases of Simpson et al. [10] and Gleyzes and Capbern [14] are selected because they were measured using laser Doppler velocimetry, an unobtrusive measurement technique. For Simpson et al. cases where $\gamma_p < 0.3$ are chosen, i.e., 144 in. $\leq x^* \leq$ 170 in. as defined in their measurement setup. Simpson et al. measured the boundary layer on a flat plate with an adjustable upper wall. Boundary layer on the upper wall was controlled by tangential blowing to ensure no flow separation occurs on the upper side of the test section. Gleyzes and Capbern

Table 1 Boundary layer parameters of profiles of Simpson et al. [10] and Gleyzes and Capbern [14]

		δ^*, [m]	δ_0^*, [m]	U_e^*, [m/s]	Re_δ	U_m	δ_0	$-\delta_0 U_m$
Simpson et al.	$x^* = 144$ in.	0.170	0.029	13.87	151471	1.258	0.170	-0.213
	$x^* = 158$ in.	0.237	0.059	13.59	206864	1.307	0.248	-0.324
	$x^* = 170$ in.	0.318	0.099	13.32	271482	1.376	0.310	-0.426
Gleyzes and Capbern	$x^*/c^* = 0.87$	0.036	0.004	50.00	115385	1.234	0.100	-0.124
	$x^*/c^* = 0.90$	0.041	0.005	50.00	132372	1.243	0.127	-0.157
	$x^*/c^* = 0.93$	0.043	0.008	50.00	137821	1.234	0.178	-0.220
	$x^*/c^* = 0.96$	0.051	0.010	50.00	163462	1.287	0.190	-0.245
	$x^*/c^* = 0.99$	0.055	0.012	50.00	176282	1.290	0.215	-0.277

velocity profiles of an undisclosed airfoil known as airfoil A at $\alpha_g = 13^\circ$ are used. At this angle of attack the surface oil flow pattern is approximately two-dimensional. The velocity profiles were measured in the ONERA/CFM F2 wind tunnel facility. For both datasets, the boundary layer has $\mathrm{d}P^*/\mathrm{d}x^* \approx 0$ and negative wall shear stress. Furthermore, the airfoil/curved surface does not ensure the development of an equilibrium boundary layer. These velocity profiles are shown in Fig. 1 in non-dimensional form. Typical boundary layer properties of the chosen dataset are presented in Table 1 along with proposed variables δ_0^*, the wall-normal position of the zero velocity and in its non-dimensional form, δ_0, and U_m, the non-dimensional maximum shear velocity.

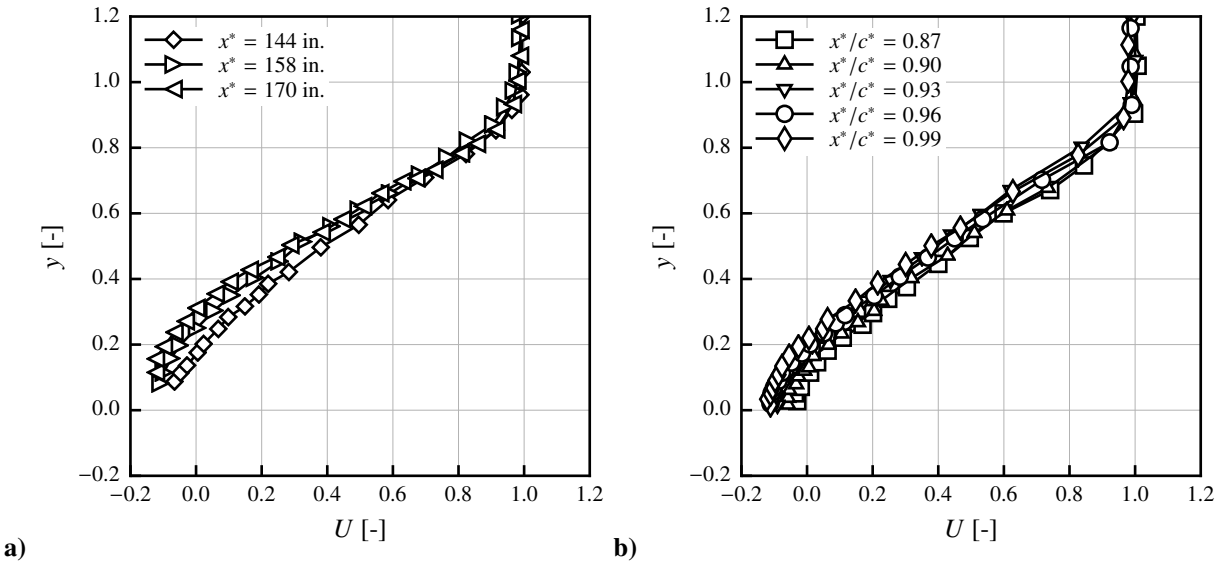

Fig. 1 Velocity profiles from a) Simpson et al.[10] and b) Gleyzes and Capbern [14]

The values of U_m were calculated from the dataset. A third-order spline function was applied to approximate a smooth mean velocity profile and the first derivative was then calculated from that function. The smoothing factor of the spline function is defined as

$$\sum_i [(U_i - f_s(x_i))]^2 \leq 0.001 \tag{13}$$

with U_i is the input data and $f_s(x_i)$ is the spline function.

The non-dimensional velocity profiles are shown in figure 2 with $U/U_m = U^+/\sqrt{\mathrm{Re}_\delta}$ as the abscissa and $(y - \delta_0)U_m = (y^+ - \delta_0^+)\sqrt{\mathrm{Re}_\delta}$ as the ordinate. The relations described above produce a similarity profile from δ_0 to δ, a distance that is approximately 70% to 80% of the boundary layer height. Although not demonstrated here, by using local parameters U_m and δ_0 the self-similarity is also useful to scale the mean streamwise velocity profile at other spanwise positions, which due to the three-dimensionality of the boundary layer may have thicker or thinner boundary layer thickness. Based on Fig. 2, a velocity profile model is proposed in the next section.

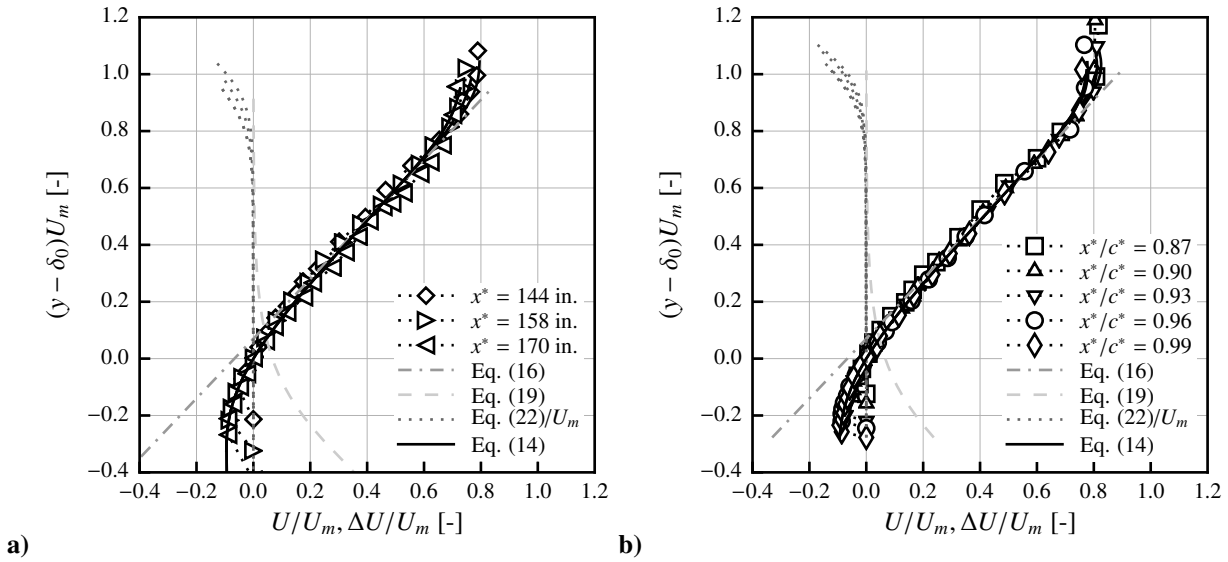

Fig. 2 Proposed velocity similarity with profiles of a) Simpson et al.[10] and b) Gleyzes and Capbern[14].

III. Velocity profile model

The velocity profile model can be defined as

$$\frac{U}{U_m} = \frac{U_l}{U_m} + \frac{\Delta U_i}{U_m} + \frac{\Delta U_o}{U_m} \tag{14}$$

where U_l/U_m is linearly dependent on $(y-\delta_0)U_m$, $\Delta U_i/U_m$ represents the near wall velocity difference, and $\Delta U_o/U_m$ represents the velocity difference near the edge of the boundary layer.

A. Linear region

The velocity profile of the linear region, U_l, can be expressed as

$$\frac{(y^+ - \delta_0^+)}{\sqrt{\mathrm{Re}_\delta}} = 1.05\frac{U_l^+}{\sqrt{\mathrm{Re}_\delta}} - 0.070 \tag{15}$$

where $\delta_0^+ = \sqrt{\mathrm{Re}_\delta} U_m \delta_0$. Equation (15) can be simplified using Eqs. (10)–(12).

$$(y-\delta_0)U_m = 1.05\frac{U_l}{U_m} - 0.070 \tag{16}$$

B. Inner region

The velocity profile just above δ_0 is modeled as a velocity difference with respect to U_l. This profile is fitted with a sigmoid function in the form

$$\frac{\Delta U_i}{U_m} = \frac{1}{a + b\exp(c\hat{\eta})} \tag{17}$$

where $\hat{\eta} = (y - \delta_0)U_m$. The constants a, b, and c were found using the boundary condition $U(\hat{\eta} = 0) = 0$.

$$\begin{aligned} \frac{\Delta U_i}{U_m}(\hat{\eta} = 0) &= \frac{U}{U_m}(\hat{\eta} = 0) - \frac{U_l}{U_m}(\hat{\eta} = 0) \\ \frac{1}{a + b} &= 0 - \frac{0.07}{1.05} \\ a &= 15 - b \end{aligned} \tag{18}$$

Substituting Eq. (18) to Eq. (17) and after least-square fitting with the measured data leads to

$$\frac{\Delta U_i}{U_m} = \frac{1}{15 - 13.53(1 - \exp(5.75\hat{\eta}))} \tag{19}$$

C. Outer region

Near the boundary layer's outer edge the velocity profile no longer scales linearly with U_m. The velocity profile in this region can be expressed as the velocity difference $\Delta U_o = U - U_l - \Delta U_i$ that takes the form

$$\Delta U_o = \frac{A}{1 + \exp[d(y - 1)]} \tag{20}$$

Where A is determined using the boundary condition $U(y = 1) = U_l + \Delta U_o = 1$ and $\Delta U_i(y = 1) = 0$.

$$\begin{aligned} U &= U_l + \Delta U_o \\ 1 &= \frac{U_m}{1.05}\left[(1 - \delta_0)U_m - 0.07\right] - \frac{A}{1 + \exp[d(y - 1)]} \\ A &= -\frac{2}{1.05}\left[(1 - \delta_0)U_m^2 - 0.07U_m - 1.05\right] \end{aligned} \tag{21}$$

and using least-square method, $d \approx 17.23$

$$\Delta U_0 = \frac{-A}{1 + \exp[-17.23(y - 1)]} \tag{22}$$

with A given in Eq. (21). Profiles of U/U_m, U_l/U_m, $\Delta U_i/U_m$, and $\Delta U_o/U_m$ are shown in Fig. 2 along with the measured data. In Fig. 2, $\Delta U_o/U_m$ vary with each dataset because ΔU_o is a function of U_m^2 and y, whereas U_l and ΔU_i are functions of U_m and $(y - \delta_0)/U_m$.

D. Relation between U_m and δ_0

Based on the mathematical functions in the previous sections, a velocity profile can be reconstructed if the following parameters are known: δ_0, U_m, and Re_δ. In this and the next section, the relationship between these parameters are explored. The relation of U_m and δ_0 is shown in Fig. 3. A mathematical model of this relation can be found by rearranging Eq. (16) into Eq. (23). By using least-squares to extrapolate Eq. (23), given the values of δ_0 and U_m in Table 1, the optimal values of y and U_l that minimizes the sum of square of the residual of δ_0 was found to be $y = 1.031$ and $U_l = 1.386$ and the sum of squared residual of δ_0 is 0.004.

$$\begin{aligned}(y-\delta_0)U_m &= 1.05\frac{U_l}{U_m} - 0.07 \\ \delta_0 &= y - \frac{1.05}{U_m}\left[\frac{U_l}{U_m} - \frac{1}{15}\right] \\ \delta_0 &\approx 1.031 - \frac{1.05}{U_m}\left[\frac{1.386}{U_m} - \frac{1}{15}\right]\end{aligned} \tag{23}$$

Furthermore, by using the boundary condition on the wall $y = 0 \rightarrow y^+ = 0$ the left hand side of Eq. (16)

$$-\delta_0 U_m < 0 \tag{24}$$

because $\delta_0 > 0$ and $U_m > 0$. Substituting Eq. (23) to Eq. (24) gives

$$\begin{aligned}-\left[1.031 - \frac{1.05}{U_m}\left(\frac{1.386}{U_m} - \frac{1}{15}\right)\right]U_m < 0 \\ 1.031U_m^2 + 0.07U_m - 1.455 > 0\end{aligned} \tag{25}$$

The first solution is a negative value of U_m, so that a requirement of the model is $U_m > 1.154$. It is important to note that this value is only an approximate value because of the least-squares method used to close Eq. (23).

E. Relation between U_m and Re_δ

From the dataset, U_m and Re_δ can be fitted with a logarithmic line expressed in Eq. (26) and shown in Fig. 4.

$$\frac{U_m}{\sqrt{Re_\delta}} = \frac{U_m^*}{U_e^*} = -0.0011\ln(Re_\delta) + 0.0168 \tag{26}$$

Hence, from both relations of $U_m(\delta_0)$ in Eq. (23) and $U_m(Re_\delta)$ in Eq. (26), a velocity profile can be modeled based on the knowledge of the value of Re_δ.

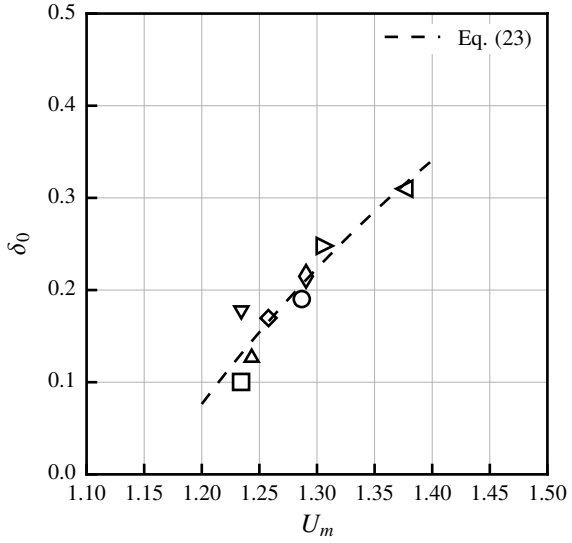

Fig. 3 Relationship between U_m and δ_0. For symbol keys see Fig. 1.

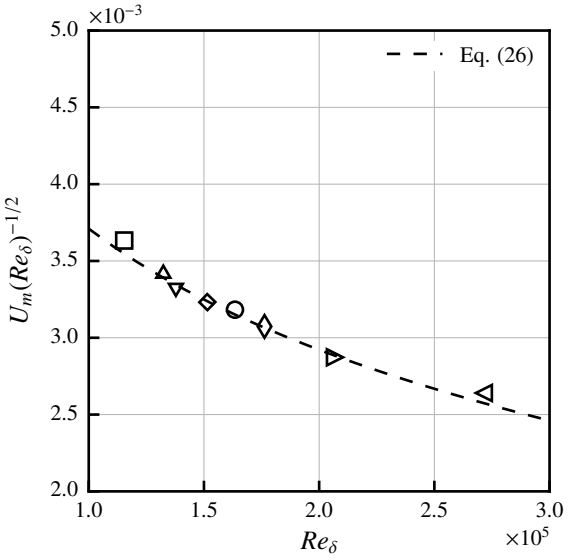

Fig. 4 Relationship between U_m and Re_δ. For symbol keys see Fig. 1.

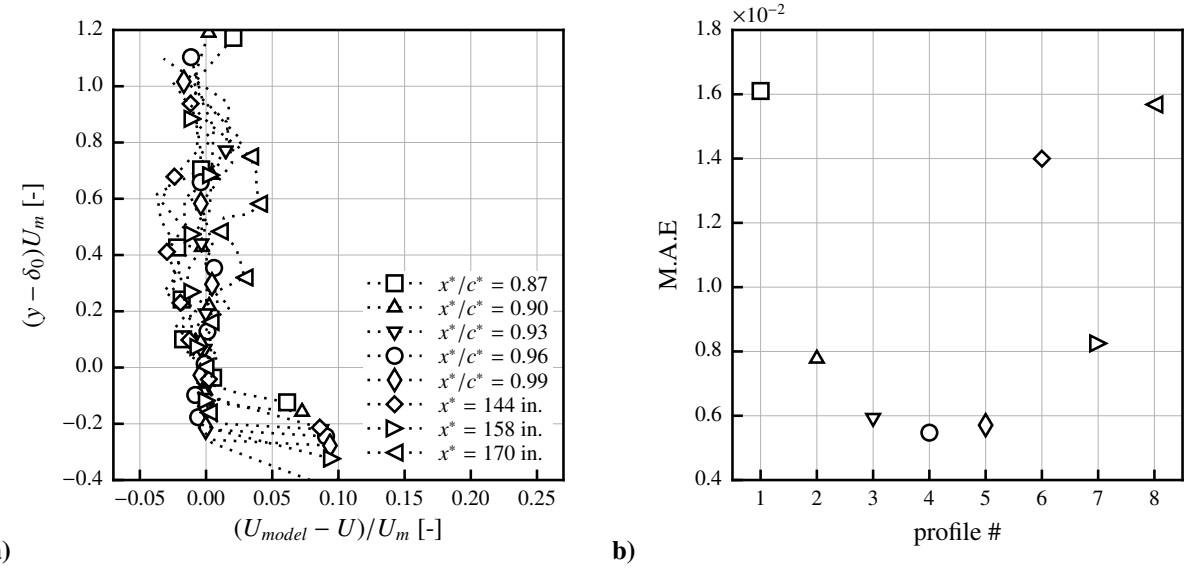

Fig. 5 a) Comparison of modeled and measured velocity profile and b) mean absolute error of the velocity profile model. For symbol keys see Fig. 1.

F. Error analysis of the proposed model

The model velocity profiles, U_{model}, calculated based on the value of Re_δ from Table 1, are compared with the measured velocity profiles, U. For $(y-\delta_0)U_m < 0$ in Fig. 5a) the velocity difference is larger than the rest of the profile because the model does not predict well the velocity next to the wall. The valid prediction range is considered for $(y-\delta_0)U_m \geq 0$.

Within the valid prediction range, the sectional error of the velocity profile is less than 5% of the measured velocity

profile. The mean absolute error of the model is defined in Eq. (27) and is shown in Fig. 5b) to be less than 2% of the local freestream velocity.

$$\text{M.A.E} = \frac{1}{N}\sum_{i=1}^{N} |U_{model}(y_i) - U(y_i)| \tag{27}$$

G. Comparison with Schüle-Rossignol model

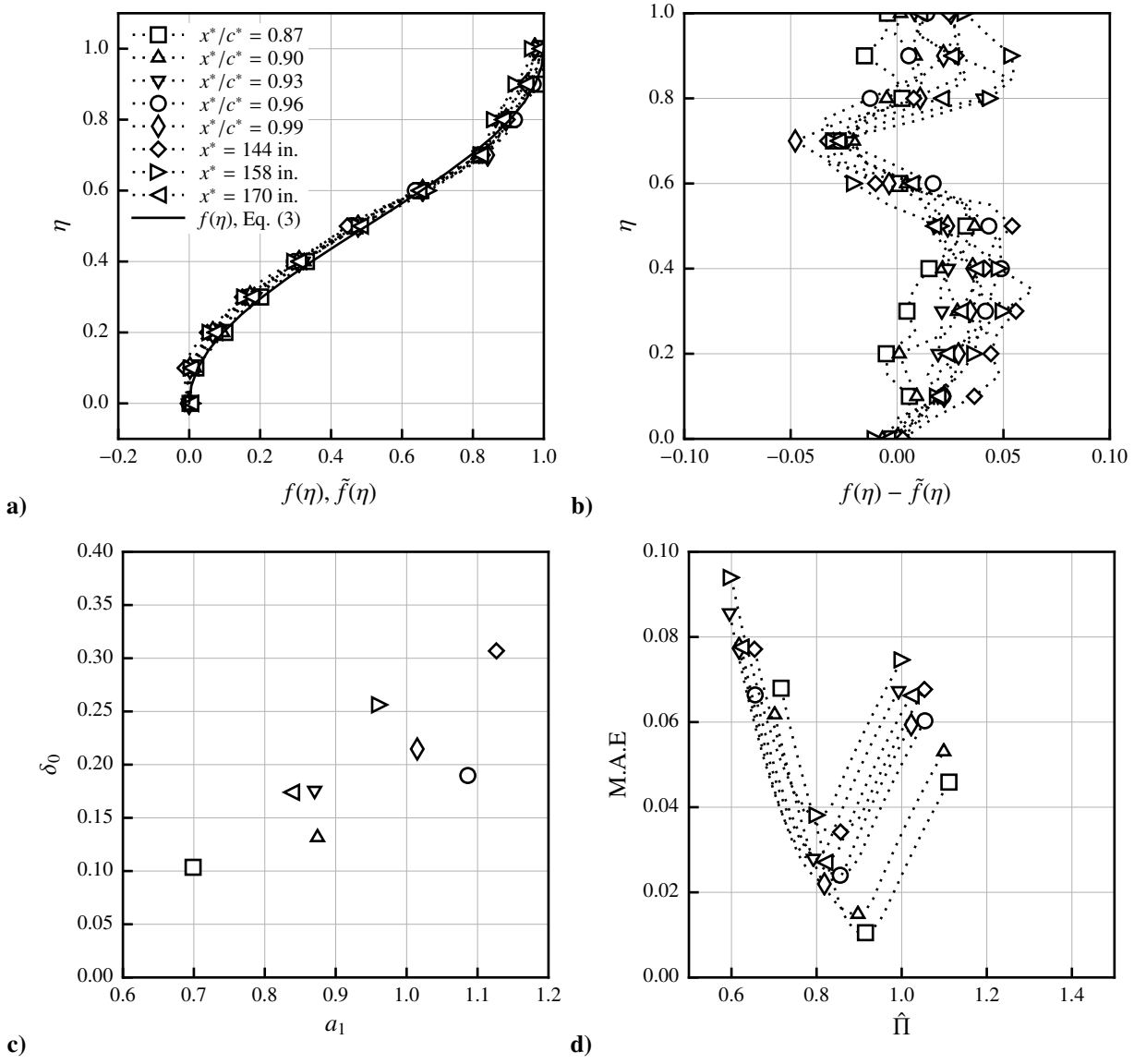

Fig. 6 Schüle-Rossignol model with dataset from Gleyzes and Capbern[14] and Simpson et al.[10]. a) self-similar velocity profiles, b) sectional error of the model, c) input parameters a_1 and δ_0, and d) Monte Carlo simulation of $\hat{\Pi}$. In d) symbols are shown as guides.

A comparison with the Schüle-Rossignol model is shown in Fig. 6. Figure 6a) shows the measured velocity profiles

in self-similar forms, $\tilde{f}(\eta) = 1/\hat{\Pi}\left[U^*(\eta)/U_e^* - g(\eta) - h(\eta, \hat{\Pi})\right]$, compared with the analytical self-similar profile, $f(\eta)$, Eq. (3). The difference, $f(\eta) - \tilde{f}(\eta)$, is between ±5% as shown in Fig. 6b). Figure 6c) shows the input parameters a_1, the mean shear at δ_0, and δ_0. The two parameters have no clear relations so that they have to be measured beforehand to use the model. Figure 6d) is the result of Monte Carlo simulations to find a value of $\hat{\Pi}$ that minimizes $f(\eta) - \tilde{f}(\eta)$. The value of $\hat{\Pi}$ was varied from 0 to 2 with uniform random distribution for 100 000 iterations, which only 20% are shown here for clarity. Figure 6d) shows the values of $\hat{\Pi}$ that produce the minimum mean absolute error is between 0.8 to 0.95 depending on the dataset. An optimal value of $\hat{\Pi} = 0.8$ can be used for engineering purposes, and this leads to a maximum error of approximately 0.04. The mean absolute error of the proposed model is approximately 0.016, a two-and-a-half fold improvement.

IV. Turbulent stress similarity

Turbulent stress profiles $\langle u^* u^* \rangle$, $\langle v^* v^* \rangle$, and $-\langle u^* v^* \rangle$ are normalized in the same steps as the turbulent velocity profiles

$$\begin{aligned}
\langle u^+ u^+ \rangle &= \frac{\langle u^* u^* \rangle}{U_m^{*2}} = \frac{\langle u^* u^* \rangle}{U_e^{*2} U_m^2} Re_\delta = \frac{\langle uu \rangle}{U_m^2} Re_\delta \\
\langle v^+ v^+ \rangle &= \frac{\langle v^* v^* \rangle}{U_m^{*2}} = \frac{\langle v^* v^* \rangle}{U_e^{*2} U_m^2} Re_\delta = \frac{\langle vv \rangle}{U_m^2} Re_\delta \\
-\langle u^+ v^+ \rangle &= -\frac{\langle u^* v^* \rangle}{U_m^{*2}} = -\frac{\langle u^* v^* \rangle}{U_e^{*2} U_m^2} Re_\delta = -\frac{\langle uv \rangle}{U_m^2} Re_\delta
\end{aligned} \tag{28}$$

The profiles $\langle uu \rangle / U_m^2 = \langle u^+ u^+ \rangle / Re_\delta$, $\langle vv \rangle / U_m^2$, and $-\langle uv \rangle / U_m^2$, are plotted with the reduced wall-normal coordinate $(y - \delta_0)U_m$ in Fig 7a)-c). A polynomial regression function of each Reynolds stress was found using least-squares to calculate the mean absolute error of the normalization. These error values are shown in Fig. 7d). The profiles $\langle uu \rangle / U_m^2$ and $-\langle uv \rangle / U_m^2$ were fitted with a 10^{th} order polynomial and the profile for $\langle vv \rangle / U_m^2$ with a 4^{th} order polynomial. The increase of the order of the polynomial is mainly due to the inflection point at $(y - \delta_0)U_m = 0.57$ for $\langle uu \rangle / U_m^2$ and at 0.65 for $-\langle uv \rangle / U_m^2$. These inflection points were determined by observing the change of sign of the second order derivative of the polynomial regression functions. The averages of the mean absolute error are 9.4×10^{-4} for $\langle uu \rangle / U_m^2$, 3.2×10^{-4} for $\langle vv \rangle / U_m^2$, and 3.0×10^{-4} for $-\langle uv \rangle / U_m^2$.

V. Similarity of the far-field acoustic pressure

The far-field noise of separated turbulent boundary layers of the DU96-W-180 airfoil was measured at three geometric angles of attack, $\alpha_g = 11°, 13°, 14.7°$ and three freestream velocities $U_\infty^* = 40, 50$, and 60 m/s. Measurements of static pressure shows that the selected α_g are pre-stall angles[30]. For a description of the measurement setup, see Schüle and Rossignol [26]. The far-field noise was measured using a directional microphone, which consists of an elliptical reflector and a microphone with its diaphragm pointed towards the reflector. The microphone was mounted on the near-focal point of the ellipse and is positioned 1.15 m below the trailing edge. By carefully positioning the

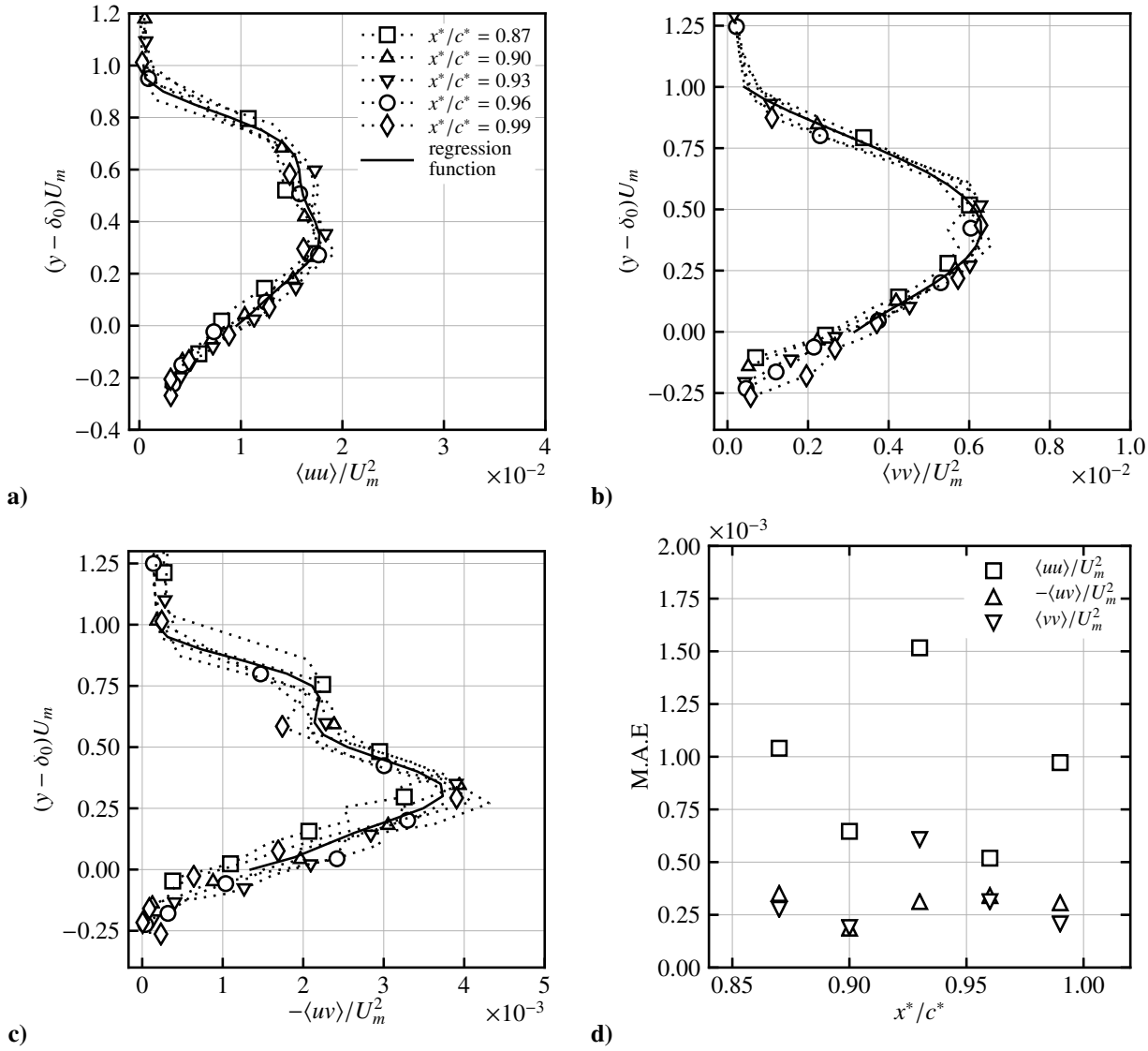

Fig. 7 Turbulent stress profiles of Gleyzes and Capbern[14]: a) $\langle uu\rangle/U_m^2$, b) $\langle vv\rangle/U_m^2$, c) $-\langle uv\rangle/U_m^2$, and d) mean absolute error of the turbulent stress models. In a)-c) selected symbols are shown for clarity.

setup, the reflector reflects noise from a noise source at the mid-span of the trailing-edge to the microphone, while other noise sources are made out-of-phase. After correction procedures (gain and spatial resolution correction, correction of extraneous noise sources, and correction of the assumed model line source [31]) the directional microphone setup provides meaningful sound pressure levels for $1 < f_m^* < 20$ kHz with signal-to-noise ratio more than 3 dB. Hot-wire anemometry was used to determine the boundary layer thicknesses at $U_\infty^* = 60$ m/s. A cross-wire probe from Dantec Dynamics model 55P61 and TSI IFA-300 data acquisition system were used to measure the chord-normal velocity profile $1\%c^*$ behind the trailing edge. It is assumed that the difference of the boundary layer profile at the point of the measurement and at the trailing-edge is negligible. Because of the directional bias inherent in the hot-wire anemometry

system, upstream moving flow cannot be distinguished from the downstream moving one. The determination of U_m was then performed by calculating the flow shear at $0.4 < y^*/\delta^* < 1$ and compared with Eq. (26). There is a maximum of 7% difference between the measured and modeled U_m as shown in Table 2, which also shows U_e^*, δ^*, Re_δ and δ_0. Surface pressure measurement was detailed in Suryadi and Herr [30]. Ultra-miniature pressure transducers from Kulite semiconductors, LQ-062-0.35BarA, were installed in the DU96-W-180 airfoil, under pinholes with the closest one to the trailing-edge at $x^*/c^* = 0.96$ on the suction side. The non-dimensional diameter of the pinhole is $d^+ = d^* u_\tau^*/\nu^* = 29$ for $\alpha_g = 0°$ and $U_\infty^* = 60$ m/s. As the value of α_g increases, d^+ decreases. According to Gravante et al. [32], the value of $d^+ > 18$ will attenuate the spectral content in the dissipative range of a zero pressure gradient turbulent boundary layer with the momentum thickness based Reynolds numbers $\mathrm{Re}_\theta = 4972 - 7076$. In this study, the attenuated spectra can be expected at $f^* > 25$ kHz, which is too large to be relevant for the present investigation. The boundary layer of the DU96-W-180 airfoil was tripped at $x^*/c^* = 0.05$ on the suction side and $x^*/c^* = 0.1$.

There is a variety of scaling laws for sound pressure levels, $L_{p,1/3}$ [31]. The experimentalists can scale their data based on U_e^*, δ_1^* or u_τ^*, δ^*, where δ_1^* is the displacement thickness. A third scaling law is proposed here based on U_e^*, δ^*, and U_m. With $\left\langle p^{*2} \right\rangle = M^{*2}\Phi_{pp}(f)$, where $\langle p^{*2} \rangle$ is the far-field sound pressure, Φ_{pp} is the power spectral density of the surface pressure and $M^* = U_e^*/a_\infty^*$ is the Mach number, the scaling of the sound pressure levels can be derived according to the scaling of $\Phi_{pp}^*(f^*)$.

A. Scaling with freestream properties

Canonically the surface pressure spectrum scales with $\Phi_{pp}^*(f^*) \propto q_e^{*2}\delta^*/U_e^*$, where $q_e^* = 0.5\rho^* U_e^{*2}$. The normalized sound pressure level is

$$\begin{aligned} L_{p,1/3;1} &= L_{p,1/3} - 50\log M - 10\log(\delta^*/l_{ref}^*) \\ St_1 &= f^*\delta^*/U_e^* \end{aligned} \tag{29}$$

where $l_{ref}^* = R^{*2}/b^*$, and $R^* = 1.15$ m is the distance of an observer (microphone) to the noise source and $b^* = 0.8$ m is the span length of the trailing-edge.

Table 2 Boundary layer parameters of Suryadi and Herr[30].

α_g,[°]	δ^*, [m]	U_e^*, [m/s]	Re_δ	δ_0	U_m	U_m[a]
11	0.020	56.9	71125	0.014	1.164	1.20
12	0.024	56.8	87385	0.195	1.279	1.27
13	0.029	59.0	109679	0.254	1.324	1.34
14	0.034	60.7	132295	0.250	1.321	1.39
14.7	0.039	61.5	153750	0.272	1.339	1.44

[a] Eq. (26)

B. Scaling with mean shear properties

In attached turbulent boundary layer the surface pressure spectrum scales with $\Phi^*_{pp}(f^*) \propto \tau^{*2}_w \delta^*_1 / U^*_e$. When the boundary layer separates, τ^{*2}_w is represented by τ^{*2}_m and δ^*_1 by δ^*, then $\Phi^*_{pp}(f^*)$ scales as $\Phi^*_{pp}(f^*) \propto \tau^{*2}_m \delta^* / U^*_e$. The second normalization of the sound pressure level is

$$\begin{aligned} L_{p,1/3;2} &= L_{p,1/3} - 10\log(M) - 40\log(U^*_m / U^*_{ref}) \\ &\quad - 10\log \delta^* / l^*_{ref} \\ St_2 &= f^* \delta^* / U^*_e = St_1 \end{aligned} \tag{30}$$

where $U^*_{ref} = 1$ m/s is an arbitrary velocity scale of unit value to normalize U^*_m.

C. Scaling with mixed properties

With the scaling introduced for the mean velocity profile in Eqs. (10) and (11), the Strouhal number is rewritten as

$$\begin{aligned} f^* &\propto \frac{U^*_e}{\delta^*} = \frac{U^+_e U^*_e U_m}{\sqrt{Re_\delta}} \cdot \frac{U_m \sqrt{Re_\delta}}{\delta^+ \delta^*} \\ f^* &\propto \frac{U^+_e}{\delta^+} \frac{U^*_e}{\delta^*} U^2_m \\ \frac{f^* \delta^*}{U^*_e} &\propto \frac{U^+_e}{\delta^+} U^2_m \\ St &\propto f^+ U^2_m \end{aligned} \tag{31}$$

where f^+ is a non-dimensional frequency and U^2_m is a non-dimensional time scale as a result of the proposed mixed scaling. The mixed scale power spectra can be derived from Parseval's theorem

$$\begin{aligned} \overline{p^{*2}} &= \int_{-\infty}^{\infty} \Phi^*_{pp}(f^*)\, \mathrm{d}f^* \\ \overline{p^2} = \frac{\overline{p^{*2}} U^*_e}{0.25 \rho^{*2} U^{*4}_e \delta^*} &= \int_{-\infty}^{\infty} \Phi_{pp}(St)\, \mathrm{d}St \\ \overline{p^2} = \frac{\overline{p^{*2}} U^*_e}{0.25 \rho^{*2} U^{*4}_e \delta^*} &= \int_{-\infty}^{\infty} \Phi_{pp}(St)\, \mathrm{d}f^+ U^2_m \\ \overline{p^2} = \frac{\overline{p^{*2}} U^*_e}{0.25 \rho^{*2} U^{*4}_e \delta^*} &= \int_{-\infty}^{\infty} U^2_m \Phi_{pp}(St)\, \mathrm{d}f^+ \end{aligned} \tag{32}$$

where $\overline{p^{*2}}$ is the fluctuating surface pressure. Defining $\Phi^+_{pp}(f^+) = U_m^2\Phi_{pp}(St) \propto U_e^* U_m^2/\rho^{*2}U_e^{*4}\delta^*\Phi^*_{pp}(f^*)$ and substituting to Eq. (29) leads to the normalization of the sound pressure level with mixed scales

$$\begin{aligned} L_{p,1/3;3} &= L_{p,1/3} - 50\log(M) + 20\log(U_m) \\ &\quad - 10\log(\delta^*/l^*_{ref}) \\ f^+ &= St_1/U_m^2 \end{aligned} \tag{33}$$

Substituting Eq. (12) to Eqs. (31) and (32) leads to simpler expressions of f^+ and the spectral scaling

$$f^+ = \frac{f^*\delta^*}{U_e^* U_m^2} = \frac{f^*\nu^*}{U_m^{*2}}, \tag{34}$$

$$\Phi^+_{pp}(f^+) = \frac{U_e^* U_m^2}{q_e^{*2}\delta^*}\Phi^*_{pp}(f^*) = \frac{U_m^{*2}}{q_e^{*2}\nu^*}\Phi^*_{pp}(f^*). \tag{35}$$

Equations (34) and (35) show that the scaled parameters f^+ is simply scaled using the viscous timescale ν^*/U_m^{*2} replacing the inertial timescale δ^*/U_e^* and Φ^+_{pp} is scaled with ν^*/U_m^{*2} and q_e^*. The present expression of the viscous timescale is analogous to that for attached turbulent boundary layers, ν^*/u_τ^{*2}, which was used to derive the surface pressure model of Goody [33].

The normalizations according to Eqs. (29), (30), and (33) are plotted in Fig. 8b)-d), respectively. A combination of symbol shapes, representing α_g, and line styles, representing U^*_∞, are used to plot the data. It shows that the proposed similarity model scales the far-field noise spectra better than the other two scaling models. In Fig. 8b) and c) the far-field noise spectra are scaled to only U^*_∞, and in Fig. 8d) they are scaled to both U^*_∞ and α_g. Focusing in the mid-frequency region in Fig. 8b), where the spectra have $(f^*)^{-4}$ dependency, the scaled spectra are shifted to a higher Strouhal number by approximately 0.1 for every increase of α_g shown. In Fig. 8c) the Strouhal shift from $\alpha_g = 11°$ to 13° is approximately 0.15, and an even larger shift from $\alpha_g = 13°$ to 14.7°. A marked improvement is shown in Fig. 8d), where the scaled far-field noise spectra are shifted to a higher f^+ only by 0.05 for every increase of α_g shown. The unscaled far-field noise spectra for constant U^*_∞ shows a broadband increase from $\alpha_g = 13°$ to $\alpha_g = 14.7°$. After normalization with Eq. (33), this is shown to be dependent on ν^*/U_m^{*2} and q_e^*. A kink at $f^+ = 1$ is observed in the far-field noise spectrum. This kink is also observable in the experimental data by Brooks et al.[27].

Measurement of surface pressure fluctuations on the suction side of the DU96-W-180 blade model had been conducted in the same facility as the measurement of far-field noise [30]. Figure 9 is the surface pressure autospectra of separated flow calculated for the 1/3 octave frequency bands, Eq. (36), and scaled using a) freestream properties, Eq. (29) and b) using Eq. (33).

$$\overline{p^{*2}}(f_m^*) = \int_{f_l^*}^{f_u^*} \Phi^*_{pp}(f^*)\,\mathrm{d}f^* \tag{36}$$

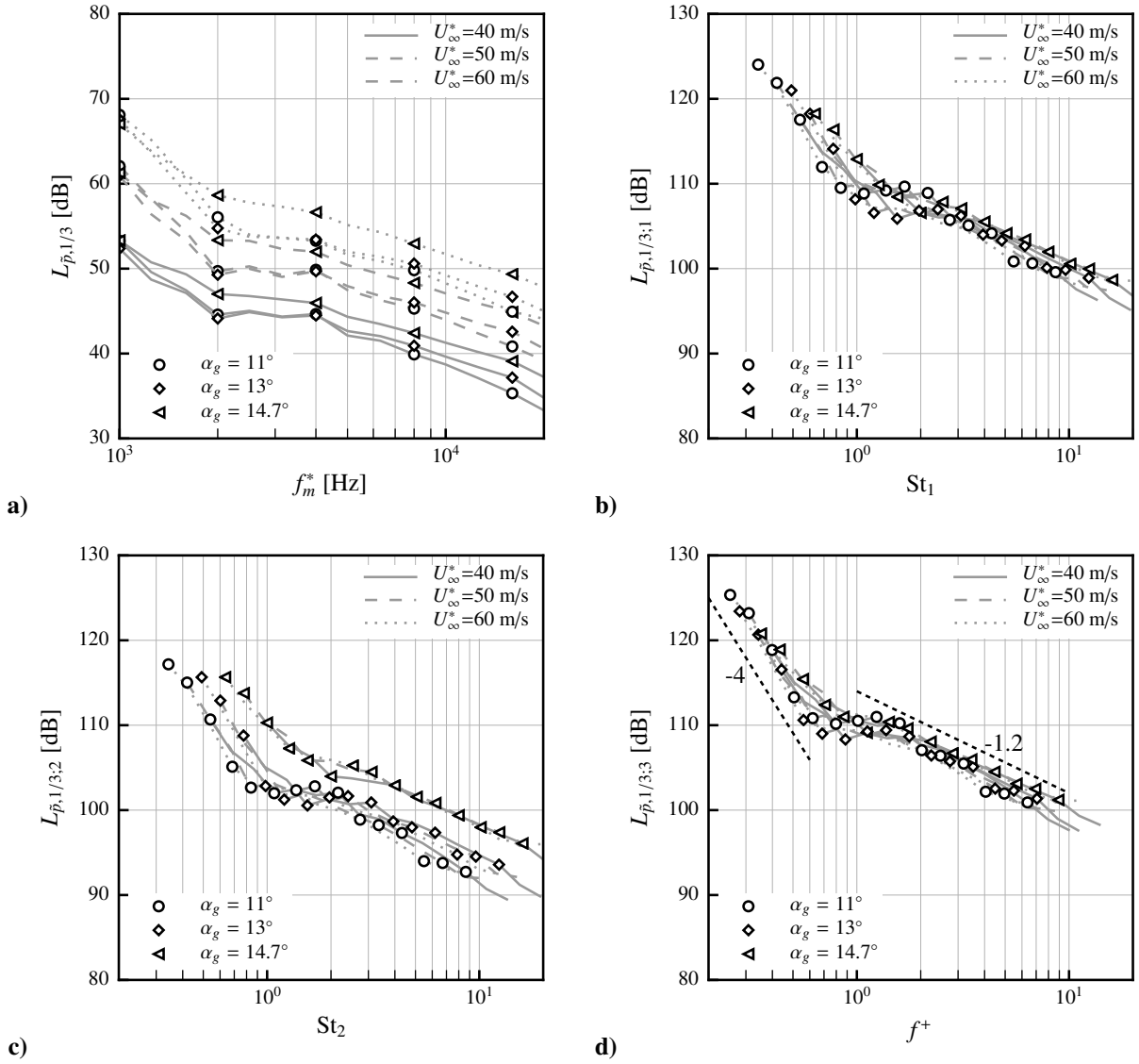

Fig. 8 Unscaled and scaled sound pressure levels a) unscaled, b) scaled using Eq. (29)**, c) Eq.** (30)**, and d) Eq.** (33)**. Every third symbols are shown for clarity.**

where $f^*_u = 2^{1/2} f^*_m$, $f^*_l = 2^{-1/2} f^*_m$, f^*_m is the center frequency and $L_{p,1/3} = 10\log(\overline{p^{*2}}/p^{*2}_{ref})$, where $p^*_{ref} = 20\ \mu$Pa is the reference acoustic pressure. The autospectra as shown in Fig. 9 can be characterized into 3 regions: (1) the low-frequency, inertial region with positive spectral slope, $St \leq 0.3$ or $f^+ \leq 0.16$, (2) the mid-frequency region, $0.3 < St \lessapprox 1$ or $0.16 < f^+ \lessapprox 0.5$, and (3) the high-frequency region with smaller spectral decay than in the mid-frequency region. Both subfigures in Fig. 9 show a dependency with α_g in the high frequency region. The change of spectral decay in the high-frequency region from the spectral decay of the mid-frequency region is attributed to the reverse flow region near the wall [15]. This implies that the increase of the spectral level in the high-frequency region from $\alpha_g = 13°$ to 14° could be due to an increase of the thickness of the reverse flow region. This is also supported by the Reynolds number

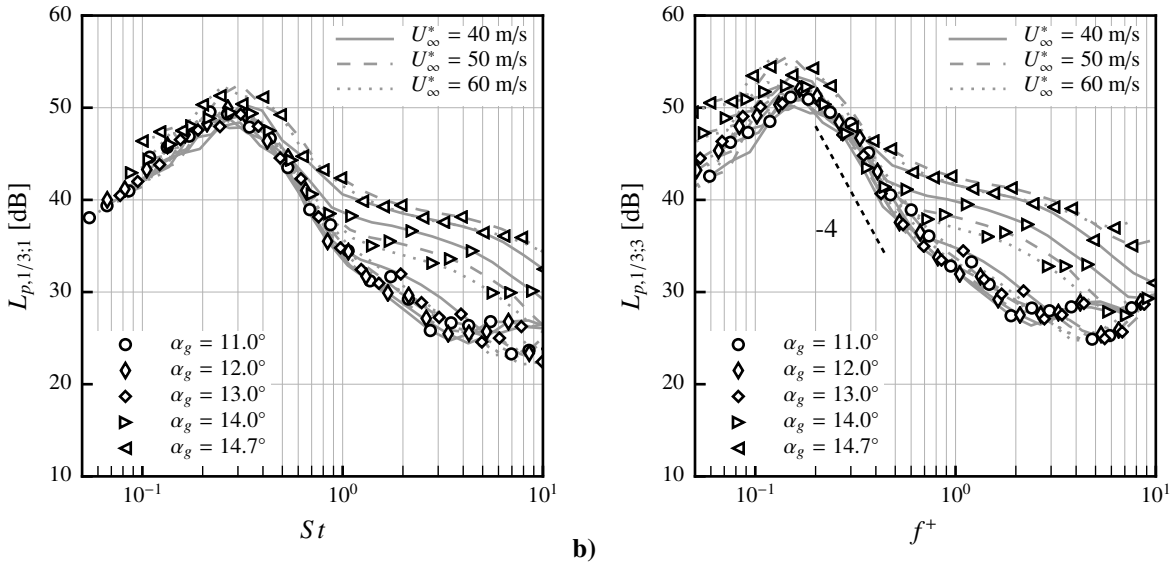

Fig. 9 Surface pressure autospectra scaled a) using freestream properties , Eq. (29) **and b) using Eq.** (33)**.**

dependency of the autospectrum at $\alpha_g = 14°$. Higher Reynolds number at constant α_g leads to thinner boundary layer and thinner reverse flow layer. A broadband frequency increase is observed for $\alpha_g = 14.7°$ and $U^*_\infty \geq 50$ m/s, which is speculated to be due to strong vorticity near the wall. It is worth noting that in this study, at $\alpha_g = 14.7°$, the ratio of the reverse flow layer and the boundary layer thickness is $\delta_0 \geq 0.27$, which will be used as a criterion for "thick" reverse flow layer.

As mentioned earlier, the scaling in Fig. 9a) is based on the inertial timescale, δ^*/U^*_e, and in Fig 9b) based on the viscous timescale, ν^*/U^{*2}_m. The maximum spectral frequency of $St = 0.3$ shows that the oscillation of the large-scale eddies is proportional to the inertial timescale and their magnitude is proportional to the inertial timescale and outer layer dynamic pressure. However, in the mid-frequency region, the two scaling methods show approximately 0.3 Strouhal number spread in Fig. 9a) and 0.1 spread for f^+ in Fig. 9b). This difference can be attributed to the inertial-to-viscous timescale ratio $R_T = (\delta^*/U^*_e)/(\nu^*/U^{*2}_m)$ that was proposed by Goody [33]. This ratio describes the relevant scales in a turbulent boundary layer which consequently describes the extent of the frequency range in the overlap region. As the value of R_T becomes large, the frequency range of the overlap region becomes wide. In zero pressure gradient turbulent boundary layer, R_T is typically in the order of 10^2 to 10^3 [31, 33, 34]. It can be easily shown from Eq. (34) that $R_T = U^2_m$, which from Table 2 is in the order of 10^0, or simply the inertial and viscous timescales are in the same order of magnitude. The small but still increasing value of R_T leads to the poor collapse of the spectra in Fig. 9b) at $f^+ \leq 0.16$. The implication is that for separated turbulent boundary layers the overlap region is absent in the surface pressure autospectrum. In the overlap region, the turbulent energy dissipation and production is in balance [35]. Its absence would indicate that for separated boundary layers the role of turbulent energy dissipation is stronger than

turbulent energy production.

The scaling based on viscous timescale shows an $(f^+)^{-4}$ dependency in Figs. 8d) and 9b) for $0.16 < f^+ \lessapprox 0.5$. This similarity implies that the mid-frequency range of the sound pressure levels in Fig. 8d) is also in the dissipative region. However, the improvement of the collapse of the sound pressure level spectra (compare Fig. 8b) with Fig. 8d)) is better than for the surface pressure autospectra (compare Fig. 9a) with Fig. 9b)), despite that the viscous and inertial timescales are in the same order of magnitude. The narrowband far-field noise is related to the surface pressure autospectrum $S^*_{FF}(f^*) \propto \ell^*_z \Phi^*_{pp}(f^*)$, where $\ell^*_z = \bar{U}^*_c r^*_z / f^*$ is the spanwise integral length scale with $\bar{U}^*_c$ is the mean convective velocity and r^*_z is the distance of two observation points in the spanwise direction. This relation assumes that $\bar{U}^*_c$ is constant in the boundary layer and it was demonstrated by Brooks and Hodgson [28] that the relation fits the far-field noise spectrum in the overlap region. Because the mid-frequency range of Fig. 8 is in the dissipative region, one cannot expect that the same assumption holds. Unfortunately, measurements of trailing-edge noise of attached turbulent boundary layers in the dissipative frequency range tend to be neglected (see, for example, Fig. 4.7, page 94 of Herr [31]), due to it being outside the upper-frequency limit of the measurement system. Therefore, a comparison of scaling approaches between the dissipative frequency range of the far-field noise of attached and separated turbulent boundary layers cannot be made.

For $f^+ > 1$ the far-field sound pressure level spectra of Fig. 8d) is independent of α_g unlike the surface pressure autospectra of Fig. 9b). Furthermore, the far-field sound pressure level decays with $(f^+)^{-1.2}$ irrespective of scaling with viscous or inertial timescale. It is speculated that the spectral contribution for the high-frequency region in Fig. 8 is from the pressure side boundary layer, where it remains attached and under the effect of favorable pressure gradient.

VI. Conclusion

The goal of this study is to find self-similar relations of the velocity profiles of a separated turbulent boundary layer, the trailing-edge noise, and the surface pressure autospectrum for future predictions. These relations were derived using mean velocity measurements at different chordwise positions of a two-dimensional airfoil and of a flat plate with adverse pressure gradient. The selected positions are downstream of the separated point, where the turbulent boundary layers have negative mean wall shear stress and zero mean streamwise pressure gradient. Trailing-edge noise and surface pressure autospectra were measured for the two-dimensional wind turbine blade model, DU96-W-180, with separated turbulent boundary layers. The trailing-edge noise was measured below the airfoil model and the surface pressure autospectrum was measured near the trailing edge on the suction side.

A scaling method for the mean streamwise velocity profile was proposed using the mean shear velocity based on the local maximum viscous shear stress, which was found to be above the wall because of flow separation. The scaled velocity profile was plotted against a reduced wall-normal coordinate, where its point-of-origin is at the reverse flow thickness. Given the limited data of the turbulent stresses, the same scaling method was applied with success. Both

mean streamwise velocity profile and profiles of turbulent stresses scale for positions above the reverse flow layer.

The same scaling parameters were used to scale the far-field noise and surface pressure autospectrum, and a comparison with the canonical scaling was presented. The proposed scaling uses the dynamic pressure based on the inertial layer parameters and the viscous timescale. Comparison of the mid-frequency range of the scaled surface pressure autospectra with the proposed scaling and with the canonical scaling method reveals that the viscous and inertial timescales are in the same order of magnitude.

The present scaling of the far-field noise collapses the spectra with respect to variations of upstream velocity and angle of attack, which suggests that the mid-frequency region of the measured far-field noise spectra is in the dissipative frequency range. In the high-frequency range, the far-field noise is independent of the angle of attack and scaling method, in contrast with the surface pressure autospectrum.

Acknowledgments

The author is grateful to GE Wind Energy GmbH, Salzbergen, Germany for funding this study between 2012 and 2015 and to Karl-Stéphane Rossignol, M.Sc for sharing his measurement data. The author is also grateful for the inputs from the reviewers.

References

[1] Schewe, G., "Reynolds-number effects in flow around more-or-less bluff bodies," *Journal of Wind Engineering and Industrial Aerodynamics*, Vol. 89, No. 14-15, 2001, pp. 1267–1289. doi:10.1016/S0167-6105(01)00158-1.

[2] Hu, H., and Yang, Z., "An Experimental Study of the Laminar Flow Separation on a Low-Reynolds-Number Airfoil," *Journal of Fluids Engineering*, Vol. 130, No. 5, 2008, p. 051101. doi:10.1115/1.2907416.

[3] Ragni, D., and Ferreira, C., "Effect of 3D stall-cells on the pressure distribution of a laminar NACA64-418 wing," *Experiments in Fluids*, Vol. 57, No. 8, 2016, pp. 1–19. doi:10.1007/s00348-016-2215-8.

[4] Tani, I., "Low-speed flows involving bubble separations," *Progress in Aerospace Sciences*, Vol. 5, 1964, pp. 70–103. doi:10.1016/0376-0421(64)90004-1.

[5] Mabey, D. G., "Separated Flow," *Journal of Aircraft*, Vol. 9, No. 9, 1972, pp. 642–645.

[6] Arena, A. V., and Mueller, T. J., "Laminar Separation, Transition, and Turbulent Reattachment near the Leading Edge of Airfoils," *AIAA Journal*, Vol. 18, No. 7, 1980, pp. 747–753. doi:10.2514/3.50815.

[7] O'meara, M., and Mueller, T. J., "Laminar separation bubble characteristics on an airfoil at low Reynolds numbers," *AIAA journal*, Vol. 25, No. 8, 1987, pp. 1033–1041. doi:10.2514/3.9739.

[8] Song, S., DeGraaff, D. B., and Eaton, J. K., "Experimental study of a separating, reattaching, and redeveloping flow over a smoothly contoured ramp," *International Journal of Heat and Fluid Flow*, Vol. 21, No. 5, 2000, pp. 512–519. doi:10.1016/S0142-727X(00)00039-4.

[9] Song, S., and Eaton, J. K., "Reynolds number effects on a turbulent boundary layer with separation, reattachment, and recovery," *Experiments in Fluids*, Vol. 36, No. 2, 2004, pp. 246–258. doi:10.1007/s00348-003-0696-8.

[10] Simpson, R. L., Chew, Y.-T., and Shivaprasad, B. G., "The structure of a separating turbulent boundary layer .Part 1 . Mean flow and Reynolds stresses," *Journal of Fluid Mechanics*, Vol. 113, 1981, pp. 23–51. doi:10.1017/S002211208100339X.

[11] Simpson, R. L., Chew, Y.-T., and Shivaprasad, B. G., "The structure of a separating turbulent boundary layer. Part 2. Higher-order turbulence results," *Journal of Fluid Mechanics*, Vol. 113, 1981, pp. 53–73. doi:10.1017/S0022112081003406.

[12] Shiloh, K., Shivaprasad, T. B., and Simpson, R. L., "The Structure of A Separating Turbulent Boundary Layer. Part 3. Transverse Velocity Measurements," *Journal of Fluid Mechanics*, Vol. 113, 1981, pp. 75–90. doi:10.1017/S0022112081003418.

[13] Dianat, M., and Castro, I. P., "Turbulence in a separated boundary layer," *Journal of Fluid Mechanics*, Vol. 226, 1991, pp. 91–123. doi:10.1017/S0022112091002306.

[14] Gleyzes, C., and Capbern, P., "Experimental study of two AIRBUS/ONERA airfoils in near stall conditions. Part I: Boundary layers," *Aerospace Science and Technology*, Vol. 7, No. 6, 2003, pp. 439–449. doi:10.1016/S1270-9638(03)00045-2.

[15] Guan, Y., Pröbsting, S., and Morris, S. C., "Unsteady surface pressure characteristics of asymmetrically beveled trailing edges," *Experiments in Fluids*, Vol. 59, No. 7, 2018, p. 118. doi:10.1007/s00348-018-2572-6.

[16] Winkelman, A. E., and Barlow, J. B., "Flowfield Model for a Rectangular Planform Wing beyond Stall," *AIAA Journal*, Vol. 18, No. 8, 1980, pp. 1006–1008. doi:10.2514/3.50846.

[17] Clauser, F. H., "Turbulent Boundary Layers in Adverse Pressure Gradients," *Journal of Aeronautical Sciences*, Vol. 21, 1954, pp. 91–108. doi:10.2514/8.2938.

[18] Maciel, Y., Rossignol, K.-S., and Lemay, J., "A Study of a Separated Turbulent Boundary Layer in Stalled-Airfoil-Type Flow Conditions," *35th AIAA Fluid Dynamics Conference and Exhibit, Toronto, Ontario. Canada*, 2005. doi:10.1007/s00348-006-0197-7.

[19] Perry, A. E., and Schofield, W. H., "Mean velocity and shear stress distributions in turbulent boundary layers," *Physics of Fluids*, Vol. 16, No. 12, 1973, pp. 2068–2074. doi:10.1063/1.1699706.

[20] Schofield, W. H., "Two-dimensional separating turbulent boundary layers," *AIAA Journal*, Vol. 24, No. 10, 1986, pp. 1611–1620. doi:10.2514/3.9491.

[21] Schüle, C. Y., and Rossignol, K.-S., "A Separated Flow Model for Semi-Empirical Prediction of Trailing Edge Noise," *New Results in Numerical and Experimental Fluid Mechanics IX*, Vol. 124, edited by A. Dillmann, H.-P. Kreplin, G. Heller, E. Krämer, U. Rist, and W. Nitsche, Springer International Publishing, 2014, pp. 639–647. doi:10.1007/978-3-319-03158-3_65.

[22] Blake, W. K., *Mechanics of Flow-Induced Sound and Vibration*, 1st ed., Academic Press, Inc., 1986.

[23] Parchen, R. R., "Progress report DRAW: A prediction scheme for trailing edge noise based on detailed boundary layer characteristics," Tech. Rep. TNO Report HAG-RPT-980023,, 1998.

[24] Herr, M., and Kamruzzaman, M., "Benchmarking of trailing edge noise computations - outcome of the BANC-II workshop," *19th AIAA/CEAS Aeroacoustics Conference, AIAA 2013-2123*, 2013, pp. 1–33. doi:10.2514/6.2013-2123.

[25] Herr, M., Ewert, R., Rautmann, C., Kamruzzaman, M., Bekiropoulos, D., Arina, R., Iob, A., Batten, P., Chakravarthy, S., and Bertagnolio, F., "Broadband Trailing-Edge Noise Predictions - Overview of BANC-III Results," *21st AIAA/CEAS Aeroacoustics Conference*, , No. June, 2015, pp. 1–31. doi:10.2514/6.2015-2847.

[26] Schüle, C. Y., and Rossignol, K.-S., "Trailing-edge noise modeling and validation for separated flow conditions," *19th AIAA/CEAS Aeroacoustics Conference, Berlin, Germany*, 2013. doi:10.2514/6.2013-2008.

[27] Brooks, T. F., Pope, S., and Marcolini, M. A., "Airfoil Self-Noise and Prediction," Tech. Rep. NASA-RP-1218, NASA Langley Research Center; Hampton, VA, United States, 1989.

[28] Brooks, T. F., and Hodgson, T., "Trailing edge noise prediction from measured surface pressures," *Journal of sound and vibration*, Vol. 78, No. 1, 1981, pp. 69–117. doi:10.1016/S0022-460X(81)80158-7.

[29] Simpson, R. L., Ghodbane, M., and McGrath, B. E., "Surface pressure fluctuations in a separating turbulent boundary layer," *Journal of Fluid Mechanics*, Vol. 177, 1987, pp. 167–186. doi:10.1017/S0022112087000909.

[30] Suryadi, A., and Herr, M., "Wall Pressure Spectra on a DU96-W-180 Profile From Low to Pre-Stall Angles of Attack," *21st AIAA/CEASAeroacoustics Conference, Dallas, Texas*, 2015. doi:10.2514/6.2015-2688.

[31] Herr, M., "Trailing-Edge Noise — Reduction Concepts and Scaling Laws," Ph.D. thesis, Technische Universität Braunschweig, Braunschweig, Germany, 2013. DLR Forschungbericht 2013-32, ISSN 1434-8454.

[32] Gravante, S. P., Naguib, A. M., Wark, C. E., and Nagib, H. M., "Characterization of the Pressure Fluctuations Under a Fully Developed Turbulent Boundary Layer," *AIAA Journal*, Vol. 36, No. 10, 1998, pp. 1808–1816. doi:10.2514/2.296.

[33] Goody, M., "Empirical Spectral Model of Surface Pressure Fluctuations," *AIAA Journal*, Vol. 42, No. 9, 2004, pp. 1788–1794. doi:10.2514/1.9433.

[34] Hu, N., and Herr, M., "Characteristics of Wall Pressure Fluctuations for a Flat Plate Turbulent Boundary Layer with Pressure Gradients," *22nd AIAA/CEAS Aeroacoustics Conference*, 2016, pp. 1–18. doi:10.2514/6.2016-2749.

[35] Pope, S. B., *Turbulent Flows*, Cambridge University Press, Cambridge, 2000. doi:10.1017/CBO9780511840531.